

# Spatially and spectrally resolved electroluminescence measurement system for photovoltaic characterisation

ISSN 1752-1416


Received on 31st October 2014

Revised on 30th December 2014

Accepted on 4th February 2015

doi: 10.1049/iet-rpg.2014.0366

[www.ietdl.org](http://www.ietdl.org)

Martin Bliss , Xiaofeng Wu, Karl Georg Bedrich, Jake William Bowers, Thomas Richard Betts, Ralph Gottschalg

Centre for Renewable Energy Systems Technology (CREST), School of Electronic, Electrical and Systems Engineering, Loughborough University, Loughborough, LE11 3TU, Leicestershire, UK

✉ E-mail: [M.Bliss@lboro.ac.uk](mailto:M.Bliss@lboro.ac.uk)

**Abstract:** A system that combines the advantages of fast global electroluminescence (EL) imaging and detailed spectrally resolved EL measurements is presented. A charge-coupled device camera-based EL imaging system is used to measure the intensity of radiative recombination of the photovoltaic (PV) device spatially resolved over its full area. A monochromator-based system is utilised to measure localised emission spectra at given points of interest. Measurements of multi-crystalline and amorphous silicon PV devices demonstrate the potential to investigate radiative defects and reveal performance variations and non-uniformities. This links inhomogeneities much closer to device physics than using camera-based EL only.

## 1 Introduction

Measurements of the current–voltage ( $I$ – $V$ ) characteristic of a photovoltaic (PV) device are important in determining its total performance and efficiency. Even though the  $I$ – $V$  characteristic can be used to identify a faulty device under test (DUT), it does not reveal any details on where the fault in the solar cells is situated. Unlike  $I$ – $V$  measurements, spatial characterisation tools such as luminescence imaging and spectroscopy, lock-in thermography and laser beam-induced current mapping identify the local performance of a solar cell in small areas and allow one to determine the area in which the defect lies [1–5]. Combined with simulation tools, one can extract more out of a measurement by investigating the effect of a defect throughout a device and on the total performance with, for example, localised  $I$ – $V$  distribution mapping [6, 7]. All-in-all spatial characterisation is vital and not only helps to improve device efficiency, but is also beneficial for the understanding of device ageing and fault development, which in turn can aid the improvement of device reliability and lifetime.

Electroluminescence (EL) imaging of PV devices has over the past years become an invaluable tool for both quality control in mass production of PV modules and solar cells, as well as in research and development of new devices and materials. EL imaging measures the radiative recombination of the DUT under forward bias by means of a camera, which makes it a very fast and non-destructive measurement method. It can highlight problem areas of a DUT, even if it seems to perform as expected, by showing minute defects such as cracks, breaks and shunts which may increase in severity in the course of the life of the device. Furthermore, measurements can be used to elucidate the spatial distribution of minority carrier lifetime and diffusion length and parasitic resistances [5, 8–10]. EL images can also be taken under reverse bias which is useful, for example, to investigate pre-breakdown sites in crystalline silicon solar cells [11, 12].

The spectral distribution of the emission is lost during standard EL imaging. However, this can provide vital characteristics of the radiative recombination mechanisms. Localised spectrally resolved EL retains the spectral content of the emitted light from the DUT at the cost of much slower measurements. Nevertheless, the additional information is useful for determining the quality of the solar cell, especially when investigating root-cause failure mechanisms. For example, using the reciprocity between EL and

quantum efficiency one can investigate the light-trapping properties in the DUT [13–15]. Furthermore, intrinsic defects such as deep trap states can be investigated. In case of multi-crystalline silicon (mc-Si), spectral EL helps to differentiate crystal boundaries from defects such as cracks, which is difficult by using charge-coupled device (CCD) camera-based EL images alone. Although fast measurement approaches have been developed in which one can differentiate defect types using an indium gallium arsenide (InGaAs) camera with additional filters [16] or light polarisation [17], most of the spectral information is still lost.

This paper presents a monochromator-based spectrally resolved EL measurement system in combination with a CCD camera-based global EL imaging system (Fig. 1). The aim is to utilise fast global EL imaging to identify areas of interest, such as defects, and to measure those specific areas using spectrally resolved EL to extract maximum useful information from the emission. In the following, the measurement system and applied measurement methods are described in detail. Measurements of a mc-Si mini-module and an amorphous silicon (a-Si) solar cell are presented and compared against reported behaviour. Finally, ongoing development options of the measurement system are discussed.

## 2 Measurement system

The main components of the measurement system, as shown in the schematic in Fig. 2, are the global EL camera system, the spectral emission measurement set-up, a  $XY$ -stage with temperature-controlled sample holder and a sample power control. The system is designed for measuring small-area devices, that is, mini-modules, cells and laboratory samples, up to a size of  $160 \times 160 \text{ mm}^2$ .

### 2.1 System integration

The  $XY$ -stage ( $200 \times 200 \text{ mm}^2$  travel length) in the interior of the light-sealed sample stage enclosure (Fig. 3) is used to change the measurement point during spectrally resolved EL measurements and move the sample into position for camera-based EL measurements.

The sample holder on top of the stage is temperature controlled via peltier elements. Secondary water cooling is used to remove excess heat from the elements. The sample temperature can be regulated

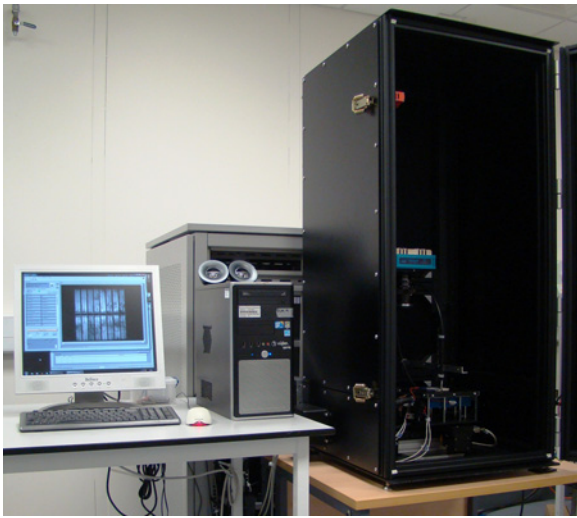


**Fig. 1** Combined EL imaging and spectral EL measurement system; the sample is positioned in the light tight enclosure on the right; behind it is a 19' rack housing the control hardware

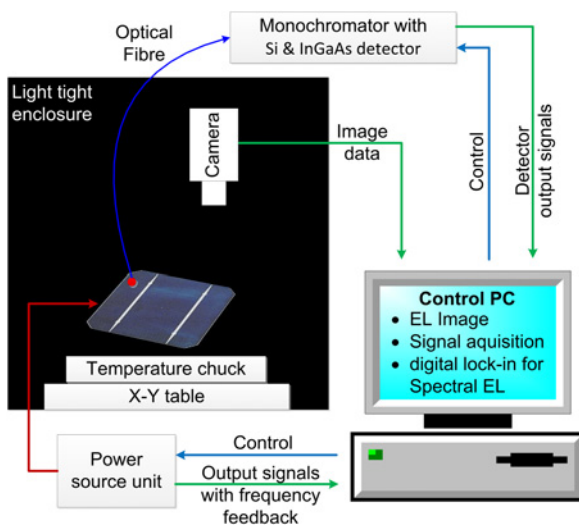


**Fig. 2** Schematic overview of the measurement system

within 15–95°C. Lower temperatures can be achieved, if necessary. This would, however, lead to water condensation on the sample and thus is normally not done. The temperature uniformity over the full sample area of the stage is  $\pm 2^\circ\text{C}$  at 95°C, measured using a thermal imaging camera.

The voltage and current input of the sample are controlled using a Keithley 2425 4-wire source unit. It provides direct current (DC) control for global EL measurements and alternating current (AC)

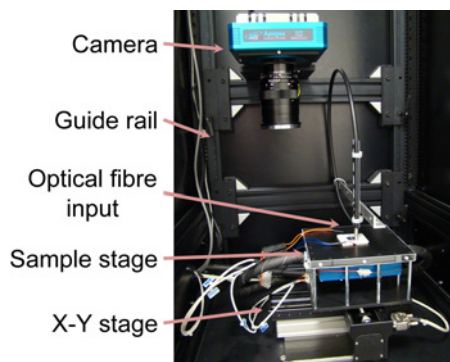


**Fig. 3** Interior of the measurement system sample stage enclosure

square wave excitation for measuring localised spectral EL emissions by the lock-in technique. Since the Keithley source unit is too slow to supply square wave AC output and deliver high-speed internal data acquisition (DAQ) at the same time, it only sources the AC output, but does not actually return any measurements. The current and voltage output to the DUT is measured externally in 4-wire configuration using a national instruments DAQ card. The AC output is timed using a trigger signal from the DAQ card supplied to the Keithley.

## 2.2 Camera-based global EL

Global EL is measured using a 16 bit Apogee Alta F-series camera with an 8.8 mega pixel silicon CCD detector. The detector is actively cooled to  $-10^\circ\text{C}$  to reduce thermal bias currents and to stabilise the spectral response. The camera optics have no zoom function as this maintains better light yield, and thus reduces exposure times. Instead, the camera is mounted on a guide rail (see Fig. 3) to adjust the distance to the DUT. The minimum focused image size is  $\sim 37 \times 28 \text{ mm}^2$  giving an image pixel resolution of  $\sim 12 \mu\text{m}$ . The background noise standard deviation (SD) was measured at six counts over a uniform area excluding defective pixels. Calculated as given in Section 3.5.8 of [18], this results into a signal-to-noise ratio (SNR) between a 90% saturated EL signal and background of up to 79.6 dB.

Filters to reduce effects of unwanted stray light are currently not used since the enclosure is light tight. Nevertheless, filters can be used to optimise image quality and aid particular measurements, for example, for evaluation of diffusion length as given in a method developed by Würfel *et al.* [10].

The source unit is used to supply a constant voltage or current to the DUT while taking the EL image. To remove the background signal, a further image is taken at same conditions without excitation of the DUT. Apart from removing the background this also largely reduces the impact of defective bright pixels from the camera detector. The remainder of the defective readings is removed by applying a  $3 \times 3$  pixel median. After this, the image undergoes a further correction for camera sensor to target distance variations because of angle of view by applying the method described in [19]. Finally, adjustments for camera lens distortions (radial and tangential) are applied. The distortions have been calibrated using the open source computer vision library [20] with images taken of square shapes in a chessboard like, black and white pattern at different positions and angles of rotation. The applied corrections improve the relation between the image taken and the actual output of luminescence from the DUT. Further calibrations can be applied as discussed in Section 4, but have not yet been included into the process.

## 2.3 Spectrally resolved EL

The system used to measure spectral EL emission measures at one fixed position at a time, which is determined by the position of the XY-stage, rather than an image of the complete sample. It utilises a dual-grating SPEX-270m monochromator with two in-house developed detectors. The first detector is used for the wavelength of 300–900 nm, that is, ultraviolet to near infrared. The second InGaAs detector is used for the 900–1700 nm range. This gives a total measurement range for defects from 0.73 to 4.1 eV. Both detectors are temperature regulated to  $-20^\circ\text{C}$ , which reduce noise, stabilise detector spectral response and reduces thermally induced self-excitation. The photodiode current is amplified by a factor  $1 \times 10^9$  via trans-impedance amplifier. A second-order 3 kHz low-pass filter reduces noise before the signal is digitalised using a 16 bit National Instruments DAQ card.

The bandwidth of the monochromator has been measured using an argon gas and mercury vapour Hg(Ar) spectral emission lamp and is 26 nm full width half maximum (FWHM) at 546 nm for the Si detector and 37 nm FWHM at 1129 nm for the InGaAs detector. The optical input for spectral EL is currently a direct fibre coupling to the sample with a measurement spot size of  $\sim 3 \text{ mm}$  diameter.

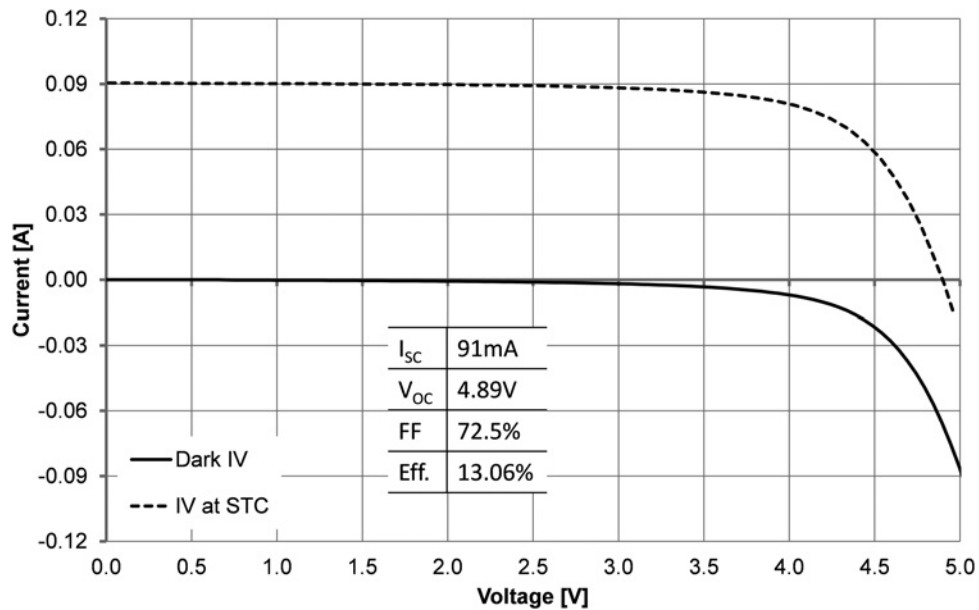


Fig. 4 I-V-curve of the c-Si sample in the dark and at STC; the main performance parameters of the I-V-curve at STC are stated

Spectrally resolved EL can be measured using AC and DC excitations of the DUT. The AC method utilises a lock-in technique in which the DUT's input current or voltage is alternated in square waveform using the source unit. The frequency is adjustable up to 200 Hz, limited by the response time of the detectors and the regulation speed of the source unit. The system utilises a digitally programmed lock-in amplifier to extract the measurement signal from the detectors at the excitation reference frequency. Dependent on which is regulated, reference signal is taken from the DUTs current or voltage measurement. A lock-in technique largely reduces background detector noise and other signal fluctuations because of external influences. The SD on the output of the digital lock-in after a 500 ms measurement interval is  $\sim 5 \mu\text{V}$  at 80 Hz, equivalent to  $\sim 5 \text{ fA}$  at both detectors.

The second method applied on the system is a DC mode in which the DUT is energised using a constant excitation current or voltage. This makes measurements more prone to external error influences as such as low-frequency noise and offset drift from the control circuit amplifiers, but would allow for measuring slow responding devices such as dye-sensitised solar cells.

Currently, the calibration of the system has been carried out using a 1 kW Tungsten Halogen standard lamp. To reduce the intensity of the light, the distance of the lamp was increased and a neutral density filter was used. This means that spectral measurements are not accurately represented in the absolute scale and may also have some distortions in the relative scale. Options for improving on this are under review in Section 4.

### 3 Device analysis

A single cell a-Si device and a mc-Si mini-module have been measured to demonstrate the functionality and as part of the validation of the measurement system.

#### 3.1 Multi-crystalline silicon

The mc-Si DUT is a commercially available mini-module containing nine cells in series on an overall size is  $60 \times 60 \text{ mm}^2$ . To give an indication of the overall quality of the test device, the

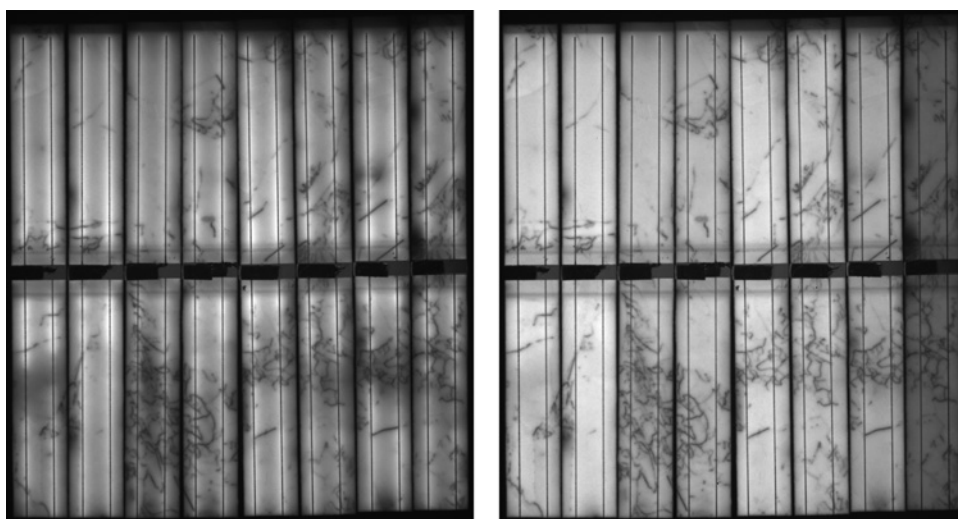
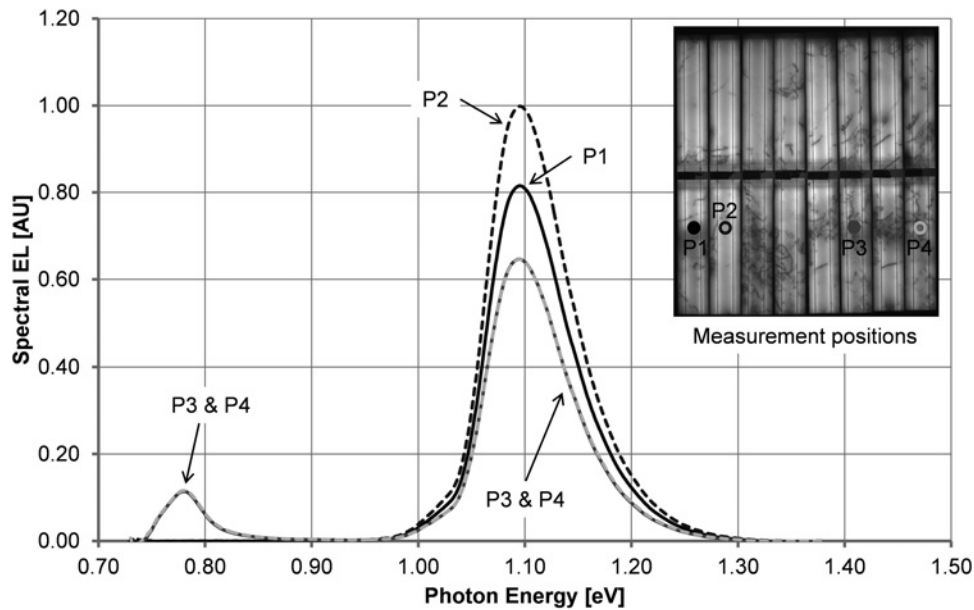


Fig. 5 Normalised EL images of mc-Si single cell; left: excitation current at  $I_{sc}$ ; right: current at 20%  $I_{sc}$ ; the absolute intensity of the signal at 20%  $I_{sc}$  is  $\sim 13$  times lower than at full  $I_{sc}$



**Fig. 6** Localised spectral EL measurements of mc-Si sample at different positions as indicated; the peak at 0.78 eV originates from the deep traps in the grain boundaries

$I$ - $V$ -curve in the dark and at standard test condition (STC) is plotted in Fig. 4.

Fig. 5 shows the global EL image of the device with an injected current at short-circuit current ( $I_{SC}$ ) of the device measured at STCs, which are the common injection current used when taking EL images, and at 20% of this value to demonstrate the change in the EL emission under lower-series resistance influences. Note that the emission profile is more uniform at low excitation current. This is as expected and because of the stronger influence of series resistance at high excitation current which induces a reduction in operating voltage in the areas away from the busbars. The change in operating voltage at the same time leads to a reduction in the current flow through the junction, and thus the emitted light from radiative recombination.

Using only the EL images is difficult to distinguish the darker lines within the cells in Fig. 5 that are not associated with the cell busbar and fingers between intrinsic defects (crystal boundaries) and extrinsic defects (breakage, cracks). Owing to the difference in

the emission spectrum, one can distinguish between them using spectrally resolved EL.

As indicated in Fig. 6, spectral emission has been measured at three points of interest. All curves show the main emission peak at the indirect bandgap of c-Si at  $\sim 1.1$  eV or 1150 nm. Furthermore, at measurement positions P3 and P4 one can see a second peak at 0.78 eV (1600 nm). This peak originates from the intrinsic deep traps in the grain boundaries of the silicon crystals and is identical to what has been reported [16, 21].

### 3.2 Amorphous silicon

The a-Si sample investigated in this paper is a large area laboratory single cell sample with an area of  $90 \times 60 \text{ mm}^2$ . This cell was chosen as it showed visible discolouration along the cell length. The cell is darker at the centre and less dark on the outer sides, which is a good indicator of non-uniform performance distribution throughout the

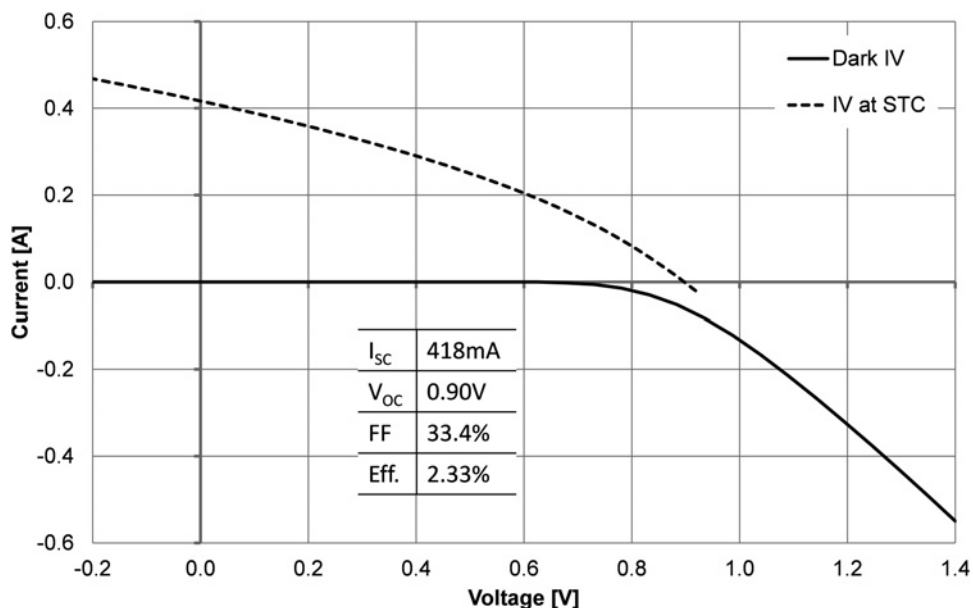


**Fig. 7**  $I$ - $V$ -curve in the dark and at STC of the a-Si sample; the influence of series resistance is clearly visible and greatly affecting the fill factor of the device



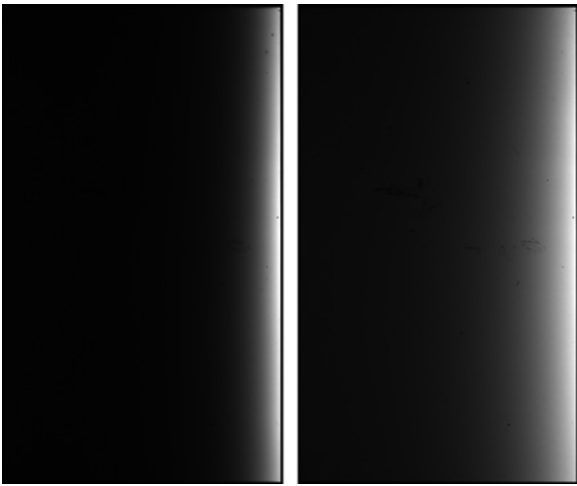


**Fig. 8** Normalised EL images of a-Si single cell; left: excitation current at  $I_{SC}$ ; right: current at 20% of  $I_{SC}$ ; the absolute scale of the image at 20%  $I_{SC}$  is  $\sim 32$  times smaller than at full  $I_{SC}$

device. From the dark  $I$ - $V$ -curve and the  $I$ - $V$ -curve at STC (Fig. 7), it is apparent that the device is suffering from a large series resistance loss, which is because of the large size of the cell.

Fig. 8 shows the global EL images of the a-Si sample at  $I_{SC}$  at STC and at 20% of  $I_{SC}$  to highlight the influences of series resistance in the cell. As one would expect from such a large thin-film single cell, it suffers from a significant lateral series resistance loss over the width of the cell between the contacts. Thus, at current injection of full  $I_{SC}$  at STC (left of Fig. 8) the signal is very strong at the positive side and drops down sharply to a very low signal at the negative contact. At 20% of  $I_{SC}$  at STC the signal drop is still visible, but not as strong. Apart from the large series resistance, the cell has a small defect in the middle part, which shows slightly darker than the surrounding area. The defect is more notable in the low excitation current image (right of Fig. 8). However, since the global EL intensity distribution is uniform along the length of the cell (top to bottom of Fig. 8), changes because of discolouration are not notable.

As detailed in Fig. 9, the spectral emission of the cell has been measured at points along the positive contact side of the cell. It is noted that the main spectral emission peak shifts between the

measurements on the left to the right of the cell from  $\sim 0.92$  to  $1.09$  eV. A second peak is visible on the right side emission spectrum at  $1.22$  eV. To note is that emission spectrum is in relative terms fairly constant across the width of the cell (i.e. direction positive to negative contact) without a shift in emission peak and changes mainly in absolute terms (Fig. 10). The spectral emission of the small defect area was measured in addition. However, it was not possible to distinguish between the variation of emission spectrum throughout the width of the cell and the defect. This may be because of the large spot size of the detector input, which is bigger than the defect area and thus defective and healthy areas are measured in a combined signal.

Very little to no emission has been measured at the effective bandgap of the a-Si device, which would be at  $\sim 1.75$  eV. Instead the dominant radiative recombination peaks have been found at much lower photon energies. In principle, the shape of the emission is comparable with reported behaviour of hydrogenated a-Si:H [22–25]. Nevertheless, the emission is dependent on many factors as such as temperature,  $i$ -layer thickness and material composition (for example, hydrogen content). The exact cause of the shift in emission spectrum has not been further investigated as part of this paper.

#### 4 Discussion and development options

Although the combined measurement system is operational, there are a wide range of options for improving the specifications of the system and thus its functionality. Those options can be found in three main areas: system set-up, calibration and interaction between global EL and spectral EL. Those are discussed as follows.

Since the measurement spot is large, an averaged emission over the optical fibre input area (3 mm diameter) was measured. This can be problematic when measuring small defect areas such as grain boundaries. Additional microscope optics can reduce the measurement spot to  $< 100 \mu\text{m}$ , which would ensure such details can be measured accurately. However, this also means that the EL signal intensity on the detectors is reduced. Furthermore, to keep the light throughput as large as possible, the bandwidth of the monochromator was kept very large. Reducing the bandwidth with smaller monochromator slits to  $\sim 4$  nm FWHM would on one hand improve the detail in the measured emission spectrum, but on the other hand reduces the signal at the detectors by a factor of  $\sim 40$ , which reduces the SNR. To be able to keep a good signal with

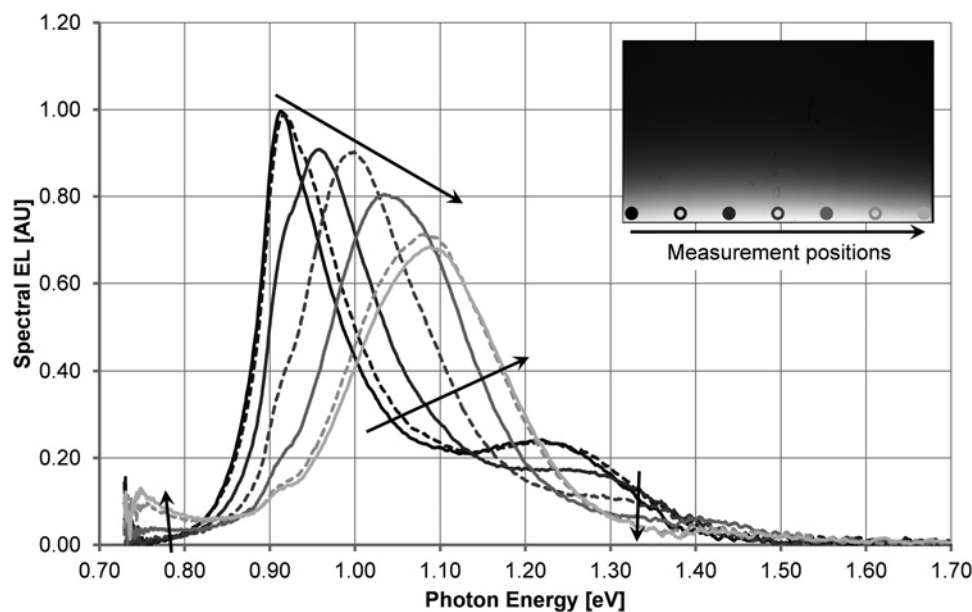


**Fig. 9** Spectral EL measurements of a-Si sample at different positions as indicated; a strong shift in the emission spectra from measurement positions on the left to the right side of the cell is visible

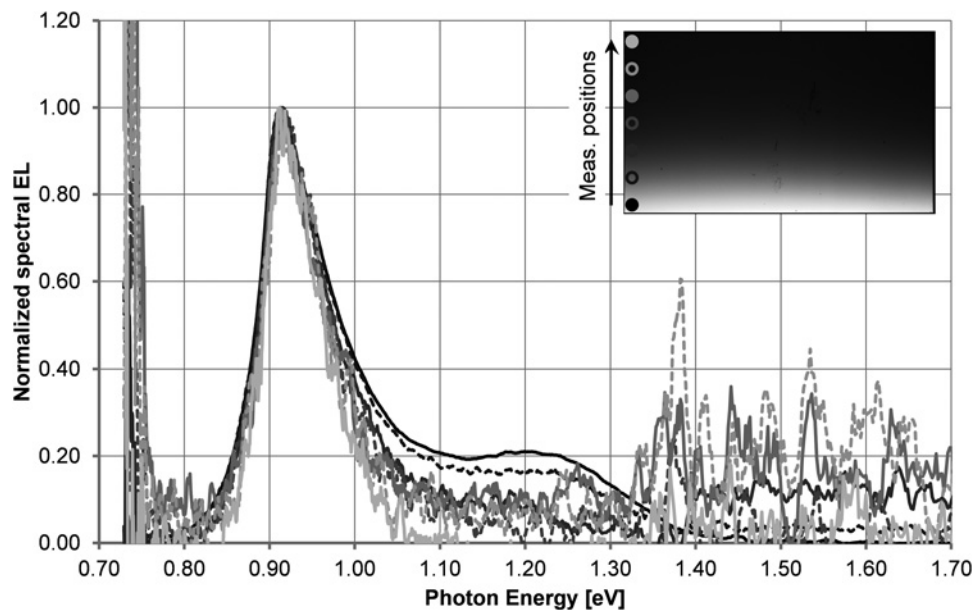


**Fig. 10** Normalised emission spectra across the width of the cell; the absolute signal peak at the positive side (black point) is 36 times larger than at negative side (grey point), relatively the dominant recombination does not shift

reduced bandwidth and measurement spot size, the optical efficiencies of the monochromator and fibre input have to be improved at the same time.

An important aspect for low measurement uncertainty is a good calibration of the measurement system. The high sensitivity of the spectral EL detectors makes its calibration a challenging task. To improve on it, one would need a low-power standard lamp or similarly as mentioned by Trupke in [26], a black-body radiator. Additionally, a camera calibration for global EL measurements is important to correct for the CCD camera optics and non-uniformities in pixel sensitivity. This can be done using a uniform light source with the spectrum of interest (ideally from a solar cell) and either a defocused lens as indicated in [19] or focused lens as reported in [27]. Finally, the linearity of system parts is an important factor to investigate.

With regard to the combined measurement system, it is important to mention that the interaction between both parts (i.e. selection of points and areas of interest for spectral EL measurements from global EL images) was at the point of writing, a manual process. The goal would be automation of this process, which requires implementation of advanced image processing methods for selecting points of interest and detecting irregularities. A range of image analysis methods have been developed in the past years, some of which are utilised in manufacturing; a review has been compiled by Israil *et al.* [28]. A particular method of interest has been developed by Tsai *et al.* [29] utilising Fourier image reconstruction.

## 5 Summary and conclusions

A combined CCD camera-based global EL and monochromatic-based spectral EL measurement system has been presented and its hardware configuration as well as the applied measurement methods have been described in detail. Demonstrative measurements of a mc-Si and a-Si devices show a comparable agreement with reported behaviour and highlight the advantage of using a combination of a fast EL imaging technique with detailed EL emission spectrum measurements. Investigating defects and other points of interest is possible with greater detail and one can yield further information on the material uniformity variations, details that otherwise might have been missed.

The full potential of the measurement system can be realised by implementing the discussed options for ongoing developments in the measurement set-up, calibration and system integration.

## 6 Acknowledgments

This work has been supported by a joint UK–India initiative in solar energy through a joint project ‘Stability and Performance of Photovoltaics (STAPP)’ funded by the Research Councils UK (RCUK) Energy Programme in UK (contract no: EP/H040331/1) and by the Department of Science and Technology (DST) in India.

## 7 References

- Vorasayan, P., Betts, T.R., Gottschalg, R.: ‘Limited laser beam induced current measurements: a tool for analysing integrated photovoltaic modules’, *Meas. Sci. Technol.*, 2011, **22**, (8), p. 085702
- Ramspeck, K., Bothe, K., Hinken, D., Fischer, B., Schmidt, J., Brendel, R.: ‘Recombination current and series resistance imaging of solar cells by combined luminescence and lock-in thermography’, *Appl. Phys. Lett.*, 2007, **90**, (15), p. 153502
- Padilla, M., Michl, B., Thaidigsmann, B., Warta, W., Schubert, M.C.: ‘Short-circuit current density mapping for solar cells’, *Sol. Energy Mater. Sol. Cells*, 2014, **120**, pp. 282–288
- Bothe, K., Ramspeck, K., Hinken, D., Brendel, R.: ‘Imaging techniques for the analysis of silicon wafers and solar cells’, *ECS Trans.*, 2008, **16**, (6), pp. 63–78
- Fuyuki, T., Kondo, H., Yamazaki, T., Takahashi, Y., Uraoka, Y.: ‘Photographic surveying of minority carrier diffusion length in polycrystalline silicon solar cells by electroluminescence’, *Appl. Phys. Lett.*, 2005, **86**, (26), p. 262108
- Fecher, F.W., Pérez Romero, A., Brabec, C.J., Buerhop-Lutz, C.: ‘Influence of a shunt on the electrical behavior in thin film photovoltaic modules – a 2D finite element simulation study’, *Sol. Energy*, 2014, **105**, pp. 494–504
- Wu, X., Bliss, M., Sinha, A., Betts, T., Gupta, R., Gottschalg, R.: ‘Distributed electrical network modelling approach for spatially resolved characterisation of photovoltaic modules’, *IET Renew. Power Gener.*, 2014, **8**, (5), pp. 459–466
- Fuyuki, T., Kitiyanan, A.: ‘Photographic diagnosis of crystalline silicon solar cells utilizing electroluminescence’, *Appl. Phys. A*, 2008, **96**, (1), pp. 189–196
- Li, B., Stokes, A., Doble, D.M.J.: ‘Evaluation of two-dimensional electrical properties of photovoltaic modules using bias-dependent electroluminescence’, *Prog. Photovolt. Res. Appl.*, 2012, **20**, (8), pp. 936–944
- Würfel, P., Trupke, T., Puzzer, T., Schäffer, E., Warta, W., Glunz, S.W.: ‘Diffusion lengths of silicon solar cells from luminescence images’, *J. Appl. Phys.*, 2007, **101**, (12), p. 123110
- Breitenstein, O., Bauer, J., Trupke, T., Bardos, R.A.: ‘On the detection of shunts in silicon solar cells by photo- and electroluminescence imaging’, *Prog. Photovolt. Res. Appl.*, 2008, **16**, (4), pp. 325–330
- Lausch, D., Petter, K., Von Wenckstern, H., Grundmann, M.: ‘Correlation of pre-breakdown sites and bulk defects in multicrystalline silicon solar cells’, *Phys. Status Solidi – Rapid Res. Lett.*, 2009, **3**, (2–3), pp. 70–72
- Kirchartz, T., Helbig, A., Rau, U.: ‘Note on the interpretation of electroluminescence images using their spectral information’, *Sol. Energy Mater. Sol. Cells*, 2008, **92**, (12), pp. 1621–1627
- Kirchartz, T., Helbig, A., Retz, W., Reuter, M., Werner, J.H., Rau, U.: ‘Reciprocity between electroluminescence and quantum efficiency used for the

- characterization of silicon solar cells', *Prog. Photovolt. Res. Appl.*, 2009, **17**, (6), pp. 394–402
- 15 Kirchartz, T., Rau, U., Kurth, M., Mattheis, J., Werner, J.H.: 'Comparative study of electroluminescence from Cu(In,Ga)Se<sub>2</sub> and Si solar cells', *Thin Solid Films*, 2007, **515**, (15), pp. 6238–6242
  - 16 Fuyuki, T., Tani, A., Tsujii, S., Sugimura, E.: 'Photographic distinction of defects in polycrystalline Si by spectroscopic electroluminescence'. 2010 35th IEEE Photovoltaic Specialists Conf., 2010, pp. 1380–1382
  - 17 Peloso, M.P., Hoex, B., Aberle, A.G.: 'Polarization analysis of luminescence for the characterization of silicon wafer solar cells', *Appl. Phys. Lett.*, 2011, **98**, (17), p. 171914
  - 18 Young, I., Gerbrands, J., Van Vliet, L.: 'Fundamentals of image processing' (Delft University of Technology, Netherlands, 1998), p. 113
  - 19 Köntges, M., Siebert, M., Hinken, D.: 'Quantitative analysis of PV-modules by electroluminescence images for quality control'. 24th European Photovoltaic Solar Energy Conf. (24th EU PVSEC), 2009, no. September, pp. 3226–3231
  - 20 Gábor, B.: 'Camera calibration with OpenCV', 2014. [Online]. Available at [http://www.docs.opencv.org/doc/tutorials/calib3d/camera\\_calibration/camera\\_calibration.html](http://www.docs.opencv.org/doc/tutorials/calib3d/camera_calibration/camera_calibration.html), accessed 16 October 2014
  - 21 Bothe, K., Ramspeck, K., Hinken, D., *et al.*: 'Luminescence emission from forward- and reverse-biased multicrystalline silicon solar cells', *J. Appl. Phys.*, 2009, **106**, (10), p. 104510
  - 22 Han, D., Wang, K., Yang, L.: 'Recombination and metastability in amorphous silicon p–i–n solar cells made with and without hydrogen dilution studied by electroluminescence', *J. Appl. Phys.*, 1996, **80**, (4), p. 2475
  - 23 Wang, K., Han, D., Silver, M.: 'The effect of photodegradation on electroluminescence in a-Si:H devices', *J. Non-Cryst. Solids*, 1993, **164–166**, pp. 595–598
  - 24 Wang, K., Silver, M., Han, D.: 'Electroluminescence and forward bias current in p–i–n and p–b–i–n a-Si:H solar cells', *J. Appl. Phys.*, 1993, **73**, (9), p. 4567
  - 25 Weber, T., Albert, A., Ferretti, N.: 'Electroluminescence investigation on thin film modules'. 26th European Photovoltaic Solar Energy Conf. (26th EU PVSEC), 2011, pp. 2584–2588
  - 26 Trupke, T.: 'Absorptivity of silicon solar cells obtained from luminescence', *Sol. Energy Mater. Sol. Cells*, 1998, **53**, (1–2), pp. 103–114
  - 27 Topic, M., Raguse, J., Zaunbrecher, K., Bokalic, M., Sites, J.R.: 'Electroluminescence of thin film solar cells and PV modules – camera calibration'. 26th European Photovoltaic Solar Energy Conf. (26th EU PVSEC), 2011, pp. 2963–2966
  - 28 Israil, M., Anwar, S.A., Abdullah, M.Z.: 'Automatic detection of micro-crack in solar wafers and cells: a review', *Trans. Inst. Meas. Control*, 2012, **35**, (5), pp. 606–618
  - 29 Tsai, D.-M., Wu, S.-C., Li, W.-C.: 'Defect detection of solar cells in electroluminescence images using Fourier image reconstruction', *Sol. Energy Mater. Sol. Cells*, 2012, **99**, pp. 250–262